Chapter 3
Enhanced photoluminescence in $CaMoO_4:Eu^{3+}$ red phosphor by Mn^{2+} co-doping

"Chapter 3 shows the enhancement of the luminescence of $CaMoO_4:4Eu^{3+}$ red phosphors with doping of limited concentrations of the transition ion Mn^{2+} ions. In this chapter, pure $CaMoO_4$, Eu^{3+} (2% to 5%) doped $CaMoO_4$, and Mn^{2+} (0.1%, 0.3% and 0.5%) co-doped 4% Eu^{3+} doped $CaMoO_4$ phosphors were synthesized by urea assisted combustion method. Structural analysis has been studied for crystal structure, phase identification, and calculation of crystallite size and microstrain. Some results of absorption spectra such as red-shift in doped and co-doped samples are discussed. This chapter discusses the effects of Mn^{2+} co-doping on the red-orange emission of Eu^{3+}-doped $CaMoO_4$. The correlation of the changed crystal field with Mn^{2+} co-doping and the luminescence of Eu^{3+} ions is discussed."

3.1 Introduction

White light emitting diodes (wLEDs) have procured commercial success over other light sources in the past decade owing to their low power consumption and increasing optical power. However, it is still important to develop high luminous efficient and cost-effective LED devices. Today, most of the commercial wLEDs are using Ce^{+3}:YAG as yellow phosphor which is coated on InGaN blue chip to give white light emission.[66–68] However, the white light emitted by these devices is primarily composed of a cold white light component due to the lack of red emission. Therefore, by introducing an efficient red-emitting phosphor, white light luminescence can be obtained.

In recent years, rare earth-doped metal molybdates have been extensively explored by the scientific fraternity because their applications are prominent and manifold.[69–73] $CaMoO_4$ have a tetragonal phase with a space group of $I4_1/a$ and finds its applications as a luminescence host in a white light-emitting diode (wLED), photo-catalysis, biomedical applications, etc.[24,73,74] $CaMoO_4$ is a self-activated phosphor which gives green light emission under UV excitation and is thus, studied as a potential phosphor in recent years. $CaMoO_4$ is also chemically and thermally stable, which adds to its advantage over other host phosphors. $CaMoO_4$ is a low-cost and easily synthesized phosphor. Many synthesis routes like solid state method [75], sol-gel[76], hydrothermal/solvothermal[22,77], and one-step spray pyrolysis[78] are used to obtain $CaMoO_4$ nano-phosphors.

It is well-studied that rare-earth doped inorganic materials have unique f-f transitions. Different rare-earth ions have been doped in $CaMoO_4$ and their color output is tuned accordingly.[79] The trivalent europium ions (Eu^{3+}) have been used as a red-emitting phosphor owing to its $^5D_0 \rightarrow {}^7F_2$ transition of 613 nm.[80] Eu^{3+} ion can be excited by UV

light; therefore it is preferred as a dopant in $CaMoO_4$. $CaMoO_4$ acts as an inorganic host antenna, which absorbs the UV range photons and then transfers the energy of the photon to the higher energy levels of the Eu^{3+} ion.[81] Although researchers have shown the energy transfer mechanism from Re^{3+} to Eu^{3+} ion in $CaMoO_4$[82], to the best of our knowledge, there are fewer reports on the effect of transition metal ion doping on the luminescence of Eu^{3+} ion in $CaMoO_4$.

In this chapter, we synthesized Eu^{3+} doped and Mn^{2+}/Eu^{3+} co-doped $CaMoO_4$ nano-phosphors by the auto-combustion method. The PL spectra of all the samples were studied and for an appropriate concentration of Mn^{2+} and Eu^{3+} ions in $CaMoO_4$, CIE coordinates were tuned for red-emitting phosphor. We have also shown that with doping of Mn^{2+} and Eu^{3+} in $CaMoO_4$, for a particular concentration, host emission is quenched while the characteristic red emission of Eu^{3+} is increased. Our prepared samples have a low synthetic price and are easy to obtain than several other commercially available rare earth-based red phosphors.

All the phosphors developed in this chapter are prepared by the urea-assisted internal combustion process, which has been described in detail in Chapter 2, in addition, all the characterization techniques and their models used in this chapter have been described in Chapter 2.

3.2 Results and discussion

3.2.1 XRD analysis

The Rietveld refined XRD patterns of CMO, E4, and EM0.3 calcined at 900^oC in the air are depicted in Fig. 3.1. All XRD patterns indicate the crystalline nature of the particles. For all samples, the observed diffraction peaks such as (101), (112), (200), (204), (312),

are indexed as a tetragonal phase with space group symmetry $I4_1/a$ (JCPDS file #85-1267 (*a=b=5.223 and c=11.429*))[83]. After the doping of Eu^{3+} and co-doping of Mn^{2+}, some distortion in bond length is observed, which is listed in Table 3.1. Distortion in bond length and other structural properties arises because the bond length of Ca—O is different from Eu—O and Mn—O. Since ionic radii and electronegativity of Eu and Mn is different from Ca[84], we observe distortion in the structure of the solid solution. Using FULLPROF software[85], the observed lattice parameters of CMO are a=b=5.2264 Å and c=11.4409 Å and volume are 312.51 $Å^3$. A further change in cell parameters and cell volume by Eu^{3+} and Mn^{2+} doping derived after refinement are also tabulated in Table 3.1 and shown in Fig. 3.2 (a). We have observed variations in the volume of the unit cell with different compositions. The Volume of the samples slightly decrease with varying concentration of Mn^{2+} in $CaMoO_4:Eu^{3+}$, the similar observation is reported by Karolewicz et al.[86] In E4, Eu^{3+} occupies the substitutional site in the crystal lattice, and since the ionic radius of Eu^{+} (1.06 Å) is less than Ca^{2+} (1.12Å).[87] We observe volume reduction and it is also justified by lattice parameter variation for E4. The variation in volume for Mn^{2+} co-doped samples (EM0.1 and EM0.3) is small from the E4 sample due to the small Mn concentration. After further doping, for the EM0.5 sample, Mn^{2+} takes a substitutional position which causes a reduction in unit cell volume and changes lattice parameters accordingly.

For the crystallite size and strain analysis in the lattice we have used Williamson-Hall (W-H) plot using the following expression[88]:

$$\beta cos\theta = c\epsilon sin\theta + \frac{k\lambda}{d} \qquad 3.1$$

where β is calculated full width at half maximum obtained by subtracting instrumental peak broadening (FWHM in radians) corresponding to the intensity peak angle θ in the XRD

pattern, θ is the peak angle of that intensity, λ is the wavelength of X-ray used in XRD Cu K_α ($\lambda = 0.154\ nm$), d is crystallite size, ϵ is lattice strain. k and c are constant where k~ 1 and c~4.

Using the W-H plot, the calculated crystallite size of the CMO is 94.51 nm and the lattice strain on the tetragonal phase structure is 0.0017. Variation of crystallite size and strain with the concentration of Eu and Mn is tabulated in Table 3.1 and shown in Fig. 3.2 (b). It is observed that with Eu doping in CMO, crystallite size increases and co-doping of Mn^{2+} in E4 reduces the crystallite size and lattice strain. The increase in the strain with Eu doping has been reported earlier also.[89] The tetragonality of all samples remains approximately the same, which confirms no change in the tetragonal phase with doping. We have not observed any Mn_2O_3 peak in the XRD pattern so there may not be the possibility of Mn being in a +3 oxidation state which is further confirmed by the XPS survey.

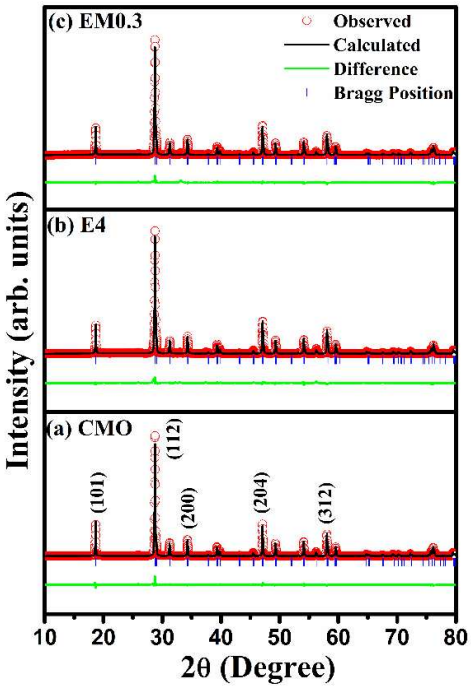

Fig. 3.1 Rietveld refined XRD patterns of **(a)** CMO, **(b)** E4, and **(c)** EM0.3 samples.

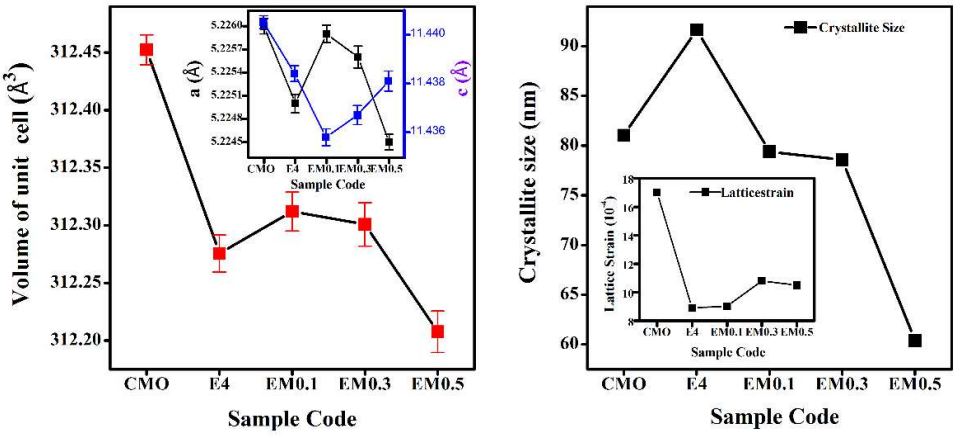

Fig. 3.2 (a) Variation in the volume of a unit cell and lattice parameters (inset) with Mn^{2+} co-doping, and **(b)** Variation in crystallite size and lattice strain (inset) with Mn^{2+} co-doping.

Table 3.1 Structural parameters obtained after Rietveld refinement XRD patterns.

Parameters	CMO	E4	EM0.3
Ca (x, y, z)	(0, 1/4, 5/8)	(0, 1/4, 5/8)	(0, 1/4, 5/8)
Mo (x, y, z)	(0, 1/4, 1/8)	(0, 1/4, 1/8)	(0, 1/4, 1/8)
O (x, y, z)	(0.1483, 0.0006, 0.2082)	(0.1479, -0.0041, 0.2105)	(0.1472, -0.0011, 0.2091)
Angles (α, β, γ)	(90, 90, 90)	(90, 90, 90)	(90, 90, 90)
Lattice parameters (Å)	a= 5.2264 ± 0.0001, c= 11.4409 ± 0.00026	a= 5.2245 ± 0.00012, c= 11.4374 ± 0.00033	a= 5.2255 ± 0.00014, c= 11.4364 ± 0.00039
V (Å^3)	312.5194 ± 0.013	312.1841 ± 0.016	312.2815 ± 0.019
χ^2	1.27	3.03	2.39
Ca-O_1	2.441	2.406	2.425
Ca-O_2	2.45	2.44	2.453
Mo-O_1	1.791	1.821	1.800
Crystallite size	94.5 nm	104.8 nm	90.62 nm
Strain (10^{-4})	17	8.92	10.8

3.2.2 TEM and EDX analysis

TEM images and selected area electron diffraction (SAED) patterns are used to study the morphological and phase analysis of the samples. EDS analysis is used for elemental analysis. TEM images of CMO and EM0.3 are shown in Fig. 3.3. The nanoparticles, shown in Fig. 3.3(a) are properly dispersed while those shown in Fig. 3.3(b) are agglomerated. The average particle size was found to be 121.03 nm for CMO and 44.09 nm for EM0.3. The well-defined diffraction rings in the SAED pattern are indexed as (004), (123), (312), (231) and (141). The inter-planar spacing from the SAED pattern is ~0.126 nm and ~0.144 nm corresponding to (141) and (231) planes.

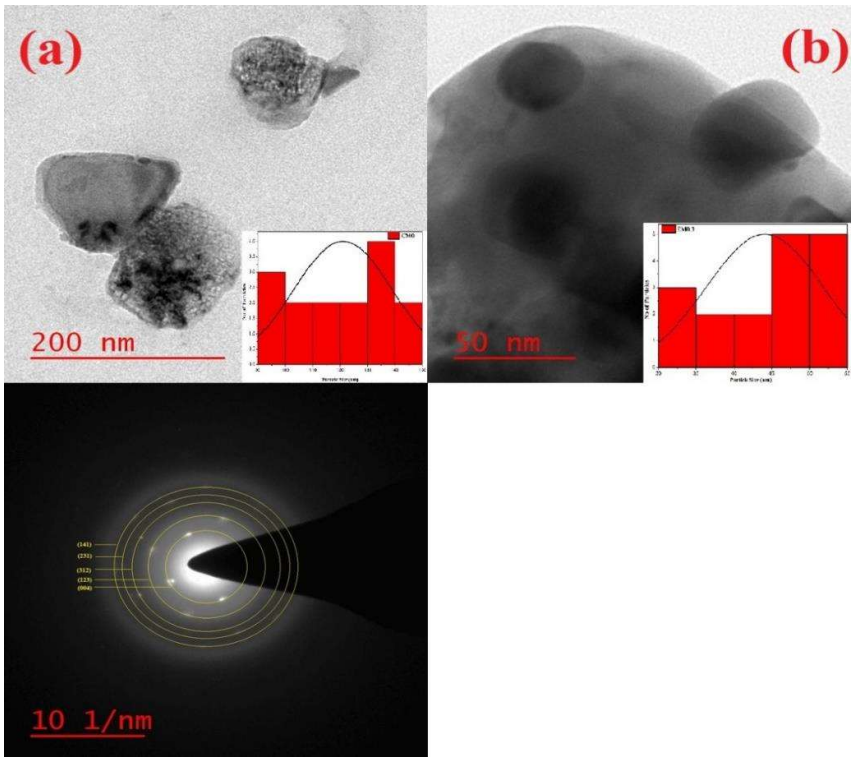

Fig. 3.3 TEM images of **(a)** CMO, **(b)** EM0.3, and **(c)** SAED pattern of EM0.3 sample.

Elemental analysis of pure CMO, E4, and EM0.3 is shown in Fig. 3.4. Table 3.2 shows the atomic and weight percentage of pure CMO, E4 and EM0.3. The EDS analysis has been

measured using a TEM instrument. We have focused on the selected area. The EDS gives approximate values of the elements present in the sample and can deviate from the actual concentration, similar variation from the actual concentration is reported by Karolewicz et al.[90] Thus, by EDS analysis we have confirmed the presence of all the elements in appropriate proportion in the samples.

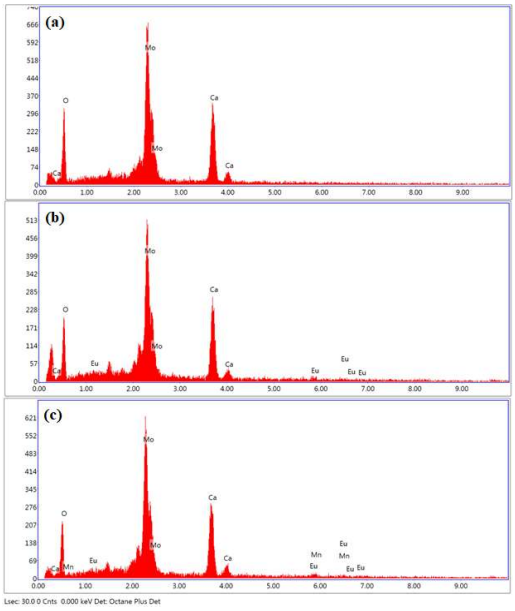

Fig. 3.4 EDX spectra of **(a)** CMO, **(b)** E4, and **(c)** EM0.3 samples.

Table 3.2 Comparative study of weight % and atomic % obtained from EDX with the taken amount used in synthesis.

Sample Code	Elements	Obtained from EDS		Taken amount	
		At.%	Wt.%	At.%	Wt.%
CMO	Ca	17.56	22.67	16.67	20.04
	Mo	13.53	41.82	16.67	47.96
	O	68.91	35.51	66.67	32
E4	Ca	19.35	22.45	16.00	18.8
	Mo	15.16	42.11	16.67	46.91
	O	64.19	29.72	66.67	31.29
	Eu	1.30	5.72	0.67	2.97

EM0.3	Ca	20.03	23.15	15.95	18.75
	Mo	15.43	42.69	16.67	46.71
	O	63.25	29.18	66.67	31.28
	Eu	1.05	4.60	0.67	3
	Mn	0.24	0.38	0.05	0.3

3.2.3 XPS analysis

The bonding states of Mn and Eu ions in CMO are further investigated from the XPS binding energy spectrum. Fig. 3.5 shows the survey scan for CMO and EM0.3. All prominent peaks of Calcium, molybdenum, and oxygen are evident in the survey scan. High-resolution XPS spectra at Ca2p, Mo3d, and O1s positions are depicted in Fig. 3.6. As depicted in the figure, two bands centered at ~346.6 eV and ~350.1 eV corresponds to Ca^{2+} $2p_{3/2}$ and Ca^{2+} $2p_{1/2}$ for CMO, respectively and bands at ~347.0 eV and ~350.5 eV corresponds to Ca^{2+} $2p_{3/2}$ and Ca^{2+} $2p_{1/2}$ for EM0.3, respectively.[91,92] We observe a blue shift of ~0.4 eV in the peak position of the two samples, this may be because Eu and Mn are substituted in the Ca site and since both are more electronegative than Ca, and therefore we observe a slight blue shift in base ion spectrum.[93] XPS scan for Ca2p confirms that calcium is in a 2+ oxidation state for pure and doped samples. The figure also shows an XPS scan for Molybdenum, revealing two broad peaks centered at ~232 eV and ~235 eV, which corresponds to Mo^{6+} $3d_{5/2}$ and Mo^{6+} $3d_{3/2}$, respectively.[91,92] Mo3d XPS scan confirms that molybdenum is in a 6+ oxidation state.

The XPS spectra of the O1s core level show asymmetric nature and are thus fitted by two peaks. The deconvoluted peaks in O1s spectra are centered at 529.89 eV and 531.68 eV for CMO, and 530.27 eV and 531.83 eV for EM0.3.[91,92] We have observed that oxygen defect

peak at ~531.6 eV increases for EM0.3. We know that oxygen is responsible for the charge transfer process in PL spectra. An increase of oxygen vacancies in EM0.3 confirms less charge transfer corresponding to $Mo^{6+} \rightarrow O^{2-}$, which will later be confirmed by PL spectra.

Fig. 3.7 shows a high-resolution XPS scan for Eu and Mn. Peaks at 1133.95 eV and 1163.9 eV corresponds to Eu^{3+} $3d_{5/2}$ and Eu^{3+} $3d_{3/2}$, respectively. We have also confirmed the presence of europium in Eu^{2+} states. Peaks at 1154.42 eV and 1124.9 eV corresponds to Eu^{2+} $3d_{3/2}$ and Eu^{2+} $3d_{5/2}$, respectively.[94] Fig. 3.7 also shows two broad peaks in the second spectrum, with their maximum at 653 eV and 641.45 eV, which confirms the presence of manganese in Mn^{2+} $2p_{1/2}$ and Mn^{2+} $2p_{3/2}$, respectively.[95] XPS scan confirms that Mn is in a 2+ oxidation state and Eu in a 3+ oxidation state in EM0.3.

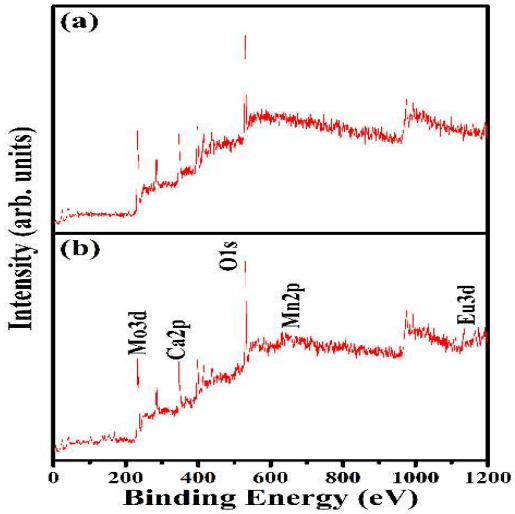

Fig. 3.5 XPS survey scan of CMO and EM0.3 samples.

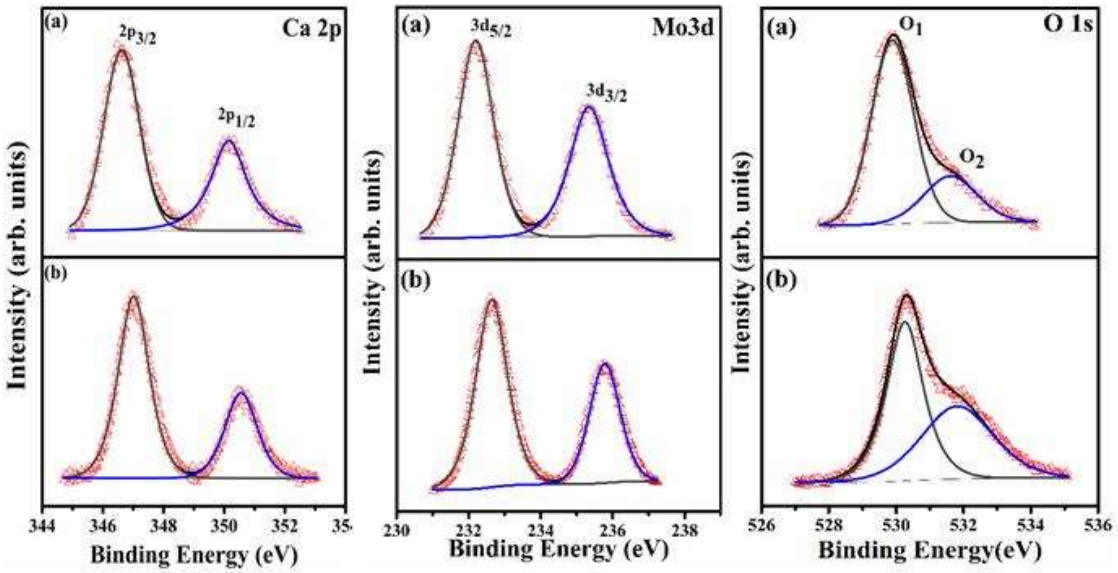

Fig. 3.6 High-resolution XPS scan of Ca2p, Mo3d, and O1s for CMO and EM0.3 samples.

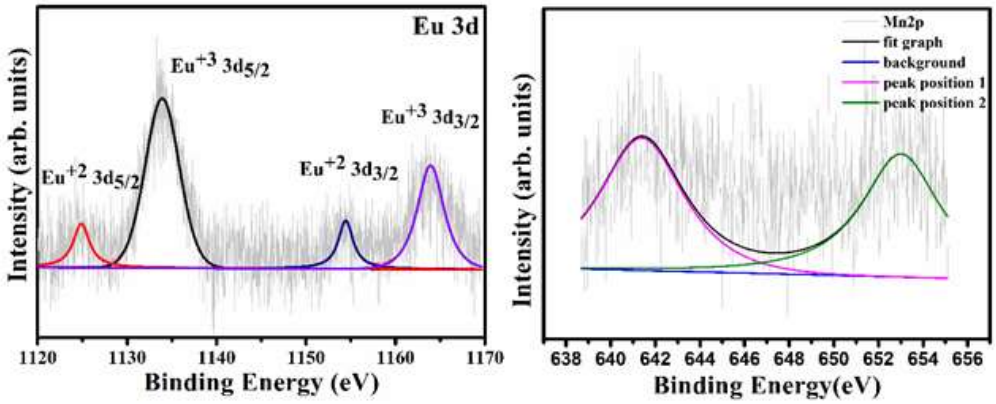

Fig. 3.7 High resolution of XPS scan of Eu3d and Mn2p for EM0.3 sample.

Table 3.3 Binding energies of all the elements obtained from XPS analysis.

Sample Code	Elements	State	B.E. (eV)
CMO	Ca 2p	Ca^{2+} $2p_{3/2}$	346.62
		Ca^{2+} $2p_{1/2}$	350.17
		Mo^{6+} $3d_{5/2}$	232.22

	Mo 3d	Mo^{6+} $3d_{3/2}$	235.32
	O 1s	$O^{2-}{}_1$	529.92
		$O^{2-}{}_2$	530.62
EM0.3	Ca 2p	Ca^{2+} $2p_{3/2}$	347.02
		Ca^{2+} $2p_{5/2}$	350.55
	Mo 3d	Mo^{6+} $3d_{5/2}$	232.65
		Mo^{6+} $3d_{3/2}$	235.77
	O 1s	$O^{2-}{}_1$	530.27
		$O^{2-}{}_2$	531.90
	Eu 3d	Eu^{2+} $3d_{3/2}$	1154.42
		Eu^{2+} $3d_{5/2}$	1124.9
		Eu^{3+} $3d_{3/2}$	1163.9
		Eu^{3+} $3d_{5/2}$	1133.95
	Mn 2p	Mn^{2+} $2p_{1/2}$	653
		Mn^{2+} $2p_{3/2}$	641.45

3.2.4 FTIR analysis

Room temperature FTIR of all prepared samples is recorded to study the vibrational modes. There are a total of 26 vibrational modes of $CaMoO_4$:

$$\Gamma = (3A_g + 5A_u) + (5B_g + 3B_u) + (5E_g + 5E_u) \quad 3.2$$

Among these 8 ($4A_u$ and $4E_u$) are infrared active and 13 (A_g, B_g, and E_g) are Raman active.[96] The recorded FTIR vibrational frequencies for different modes of CMO, E4, EM0.1, EM0.3 and EM0.5 samples within the wavelength range 400 cm^{-1} to 4000 cm^{-1} are shown in Fig. 3.8 and are listed in Table 3.4. The E4 sample has two major peaks in the fingerprint region (400 cm^{-1} to 1500 cm^{-1}). The intense absorption band centered at 772 cm^{-1} corresponds to E_u and A_u modes, the anti-symmetric stretching vibrations of $[MoO_4]$ tetrahedral clusters. The band at 434 cm^{-1} corresponds to a less intense A_u mode which is correlated to anti-

symmetric vibrations of O–Mo–O angles.[97] This confirms the tetragonal structure of all samples. We have not observed any shift in the two bands involving Mo and O.

In the 1500 cm^{-1} to 4000 cm^{-1} regions, some other peaks are also observed in the FTIR spectrum. The Peak at ~2358 cm^{-1} is attributed to carbon dioxide from the atmosphere.[98]

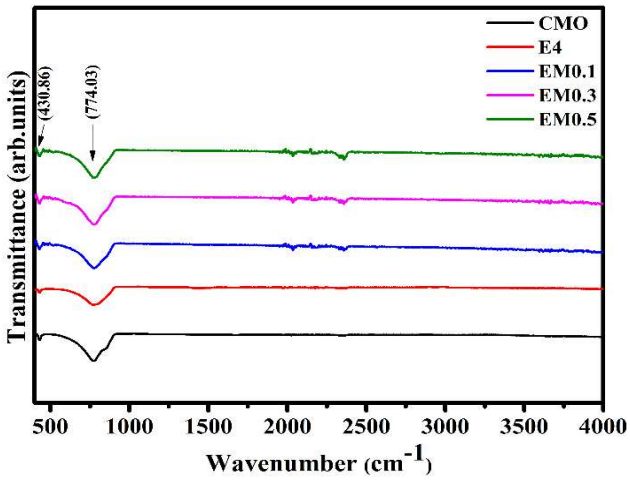

Fig. 3.8 FTIR spectra of CMO, E4, EM0.1, EM0.3 and EM0.5 samples.

Table 3.4 Vibrational band of CMO, E4, EM0.1, EM0.3 and EM0.5 samples

Sample code with respective wave numbers (cm^{-1})					**Vibrational bond**
CMO	**E4**	**EM0.1**	**EM0.3**	**EM0.5**	
430.86	430.86	430.86	430.86	430.86	Bending of Mo-O
774.03	774.03	774.03	774.03	774.03	Stretching of O-Mo-O
2358.66	2355.23	2357.55	2356.5	2356.92	Stretching of O=C=O

3.2.5. Absorption analysis

The absorption spectra of CMO, E2, E3, E4, and E5 in the wavelength range from 200 to 800 nm are shown in Fig. 3.9(a). It is observed that CMO spectra have a wide absorption band centered at 291 nm, which is because of the charge transfer from the O^{2-} ion to the Mo^{6+} ion. We observe a shift in absorption band peak from 291 nm to ~315 nm for Eu^{3+}

doped CMO samples. Again the absorption band in the case of Eu^{3+} doped CMO is ascribed to the charge transfer transitions from the O^{2-} ion to the Eu^{3+} ion. The other two transitions are observed at 465 nm and 536 nm which are due to $^7F_0 \rightarrow {}^5D_2$ and $^7F_0 \rightarrow {}^5D_1$, respectively. The latter two transitions are electric dipole and hypersensitive transitions.[99] We have observed the broadening in the absorption spectrum for Mn^{2+} co-doped samples, which is shown in Fig. 3.9(b).

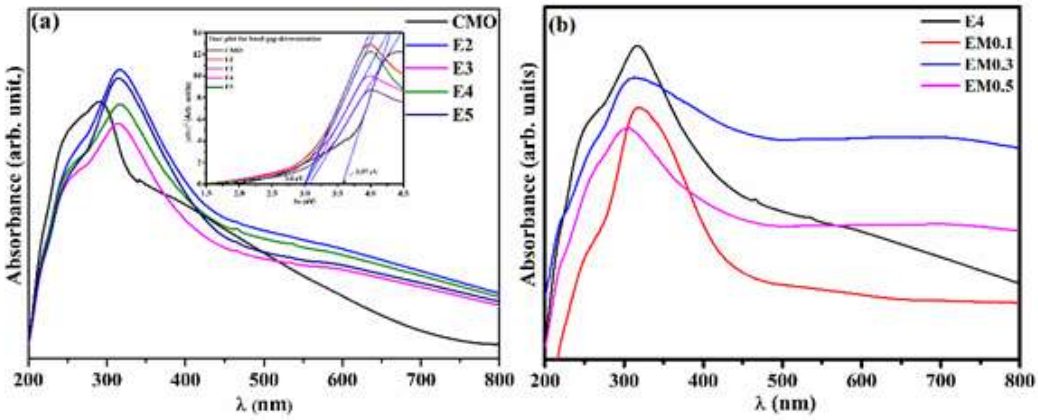

Fig. 3.9 (a) Absorption spectra of Eu^{3+} doped $CaMoO_4$. Inset: Tauc plot for obtaining bandgap and **(b)** Absorption spectra of Mn^{2+} co-doped Eu^{3+} doped $CaMoO_4$.

The optical band gap of the synthesized phosphors is calculated using the well-known Tauc equation[100,101];

$$\alpha h\nu = A(h\nu - E_g)^n \qquad 3.3$$

Where α is the absorption coefficient, ν is the photon frequency, h is Planck's constant and A is a constant. The value of exponent n for CMO is ½ because its electronic transitions are direct allowed type.[100, 101] The optical band gap was calculated by plotting $(\alpha h\nu)^2$ versus photon energy $(h\nu)$ of the phosphors. The inset in Fig. 3.9(a) shows the calculated band gap of phosphors by extrapolating the linear portion of the spectra to $(\alpha h\nu)^2 = 0$. The

calculated band gap of CMO is estimated to be 3.3 eV. With doping of Eu^{3+} ion in CMO, we observe a shift in band edge and it is found to be 3.0 eV, this may be due to an increase in covalent bond length between Mo—O due to Eu^{3+} doping. It is known from the literature that $4f^6$ electrons of europium increase the covalent bonding between cation and oxygen, which in our case is between Mo and O. Increase in the bond length of Mo—O for Eu^{3+} doped sample is also listed in Table 3.1. This increase in covalent bond length between Mo—O reduces the band gap of Eu^{3+} doped samples.[102]

3.2.6 Photoluminescence analysis

3.2.6.1 Excitation (PLE) spectra

Excitation spectra of all samples have been recorded by observing the variation of luminescence intensity with excitation wavelength. Excitation spectra of $CaMoO_4:xEu^{3+}$ doped nano-phosphors are obtained by monitoring the $^5D_0 \rightarrow {}^7F_2$ transition emission of Eu^{3+} at about 615 nm, shown in Fig. 3.10(a). The excitation band from 230 to 320 nm is recorded which results from the overlap of the ligand-to-metal charge transfer (LMCT) band and charge transfer band (CTB). The CTB is the result of charge transfer from the filled 2p orbital of O^{2-} to the partially filled orbital of the Eu^{3+} ions ($O^{2-} \rightarrow Eu^{3+}$) which is because Eu^{3+} is lacking only one electron to achieve a stable half-filled shell. CTB signifies the transfer of an electron from the neighbouring atoms to the Eu^{3+} ion, thereby reducing it to Eu^{3+} and LMCT band arises due to the combination of the ligand to metal charge transfer $O^{2-} \rightarrow Mo^{6+}$.[89] The intra f—f transitions of Eu^{3+} around 367 nm ($^7F_0 \rightarrow {}^5D_4$), 376 nm ($^7F_0 \rightarrow {}^5G_3$), 382 nm ($^7F_0 \rightarrow {}^5G_4$), 395 nm ($^7F_0 \rightarrow {}^5L_6$), 415 nm ($^7F_0 \rightarrow {}^5D_3$), 464 nm ($^7F_0 \rightarrow {}^5D_2$) and 534 nm ($^7F_0 \rightarrow {}^5D_1$) are also observed as reported earlier[103,104] (inset of Fig. 3.10(a)).

Fig. 3.10(b) shows excitation spectra for Mn^{2+} co-doped E4 nano-phosphors in the wavelength range 225 nm to 350 nm at an emission wavelength of 615 nm. It is observed that the intensity of the CTB increases up to 0.3% Mn^{2+} concentration and then starts to decrease until we reach 1% Mn^{2+} concentration (not shown in graph). We can deduce that a small concentration of Mn^{2+} helps to effectively transfer charge from O^{2-} to the partially filled orbitals of the Eu^{3+} ions.

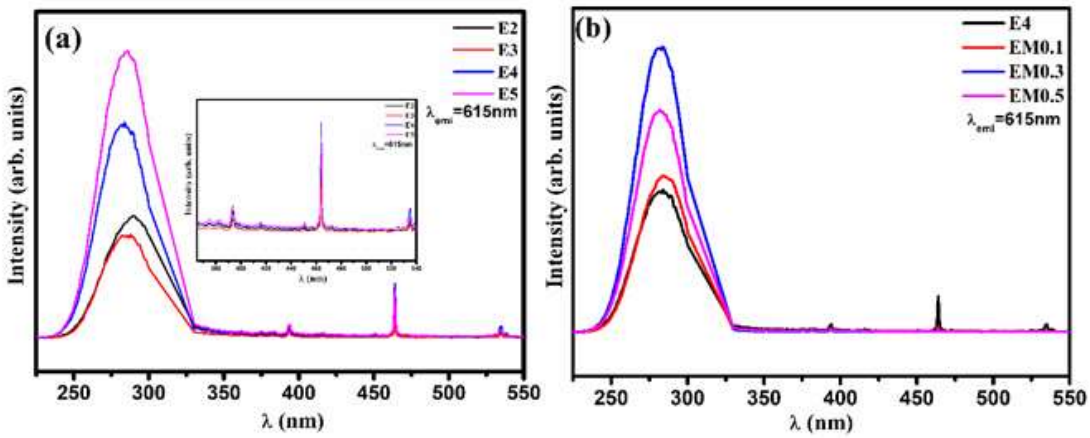

Fig. 3.10 PL excitation spectra of **(a)** Eu^{3+} doped $CaMoO_4$ and **(b)** Mn^{2+} co-doped Eu^{3+} doped $CaMoO_4$ phosphors.

3.2.6.2 Emission (PL) spectra

Emission spectra are recorded by fixing the excitation wavelength. Emission spectra of Eu^{3+} doped CMO nano-phosphors are shown in Fig. 3.11(a) under 290 nm excitation. The spectrum of CMO phosphor shows broad band emission in the range 425 nm to 575 nm, which is due to the transfer of an electron from the excited state to the ground state of the host.[23,105] It is observed that there is variation in the intensity of the peak, which signifies how effectively that process of charge transfer takes place. The peak intensity is minimum for E4 concentration. The inset of Fig. 3.11(a) shows spectra in the range from 600 nm to 725 nm. Peaks are observed around 615 nm which are due to the $^5D_0 \rightarrow {}^7F_2$ transition. The

$^5D_0 \rightarrow {}^7F_2$ transition is an electric dipole transition and its dominance in the spectrum conveys that Eu^{3+} is located in a site without inversion symmetry.[89,106] The intensity of $^5D_0 \rightarrow {}^7F_2$ is much influenced by the local symmetry of the Eu^{3+} ion. Other peaks are observed around 652 nm ($^5D_0 \rightarrow {}^7F_3$), and 702 nm ($^5D_0 \rightarrow {}^7F_4$), which are all electric dipole transitions.[99,106] All observed emission peaks due to Eu^{3+} transitions have been reported by Guzik et al. for Eu^{3+} doped $CdMoO_4$ phosphors.[103] The Emission intensity of the broadband around 425 nm to 575 nm is minimum for E4 consequently to which it is observed that all peaks in the range 600 nm to 725 nm increase up to E4. This observation infers that for E4 there is an effective charge transfer from the host to Eu^{3+} levels.

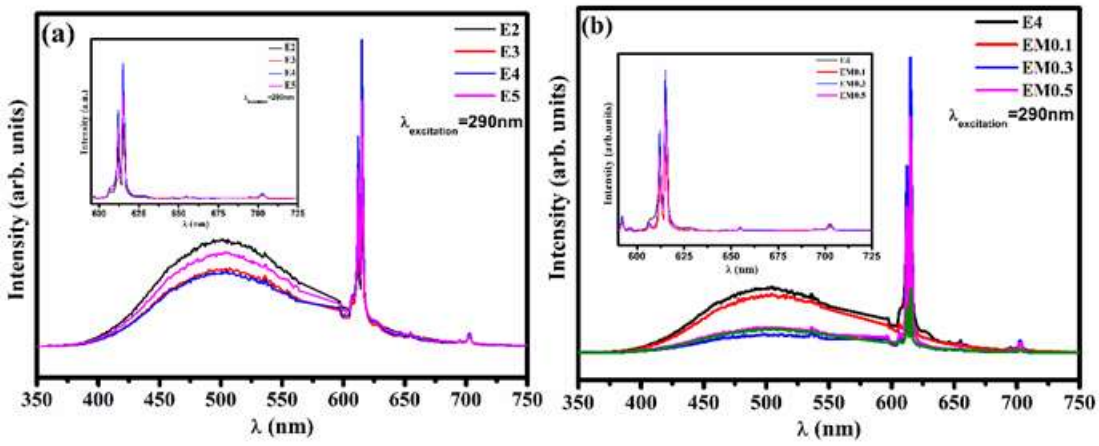

Fig. 3.11 PL emission spectra of **(a)** Eu^{3+} doped $CaMoO_4$ and **(b)** Mn^{2+} co-doped Eu^{3+} doped $CaMoO_4$ phosphors.

Fig. 3.11(b) shows PL emission spectra for Mn^{2+} co-doped E4 nano-phosphors under 290 nm excitation wavelength. All samples show intense $^5D_0 \rightarrow {}^7F_2$ (615 nm), $^5D_0 \rightarrow {}^7F_3$ (652 nm), and $^5D_0 \rightarrow {}^7F_4$ (702 nm) emission lines and a broad band around 425 nm to 575 nm.[99,107,108] Our observations depict that the electric dipole transition is dominant over the magnetic dipole transition for all samples. The emission intensity of the broadband around 425 nm to 575 nm decreases with Mn^{2+} concentration in the E4 phosphor. Consequently,

the intensity of, 615 nm, 654 nm and 702 nm all increase up to EM0.3. This increase in peak intensity may be due to substitutional and crystal field effects. Similar behaviour has been reported for Zn^{2+} doped $CaMoO_4:Eu^{3+}$.[109] Mn^{2+} doping may change the crystal field around Eu^{3+} which leads to electric dipole transition. Thus, a small concentration of Mn^{2+} improves luminescence by increasing electric dipole transitions. It is well known that electric dipole transitions are dependent on the distortion in the local environment around Eu^{3+}, to check this we have calculated the asymmetric parameter for E4, EM0.1, EM0.3 and EM0.5. The asymmetric parameter (A_s) is calculated by following well-known relation[109,110]:

$$A_s = \frac{Area\ under\ the\ major\ peak\ corresponding\ to\ electric\ dipole\ transition}{Area\ under\ the\ peak\ corresponding\ to\ magnetic\ dipole\ transition} \qquad 3.4$$

It is found that A_s is the maximum for EM0.3 phosphor, i.e. 23.5, and reduces as we further increase Mn^{2+} ion concentration in E4 phosphor.

3.2.7 Chromaticity parameters

Fig. 3.12 shows the Chromaticity diagram and Commission Internationale de l'Elcairage (CIE) Coordinate of the samples E4 and EM0.3 annealed at 900 ^oC which is calculated from PL spectra (Eu^{3+} emission spectra range from 580 nm to 800 nm) excited at 290 nm. The calculated CIE coordinate of E4 is (0.670, 0.329) which corresponds to the red phosphor. For EM0.3 CIE coordinate is (0.674, 0.326) and it shifts more toward the red color in the chromaticity diagram. The chromaticity diagram shows the enhancement in red color via the co-doping of Mn^{2+} ions. Correlated color temperature (CCT) gives information about that temperature corresponding to the radiation of that color. For both samples, E4 and EM0.3, the correlated color temperature (CCT) is 1000K. In addition, the color purity of the phosphor is evaluated in percentage to measure the monochromaticity, which is

99.5% for E4 phosphor and 99.9% for EM0.3 phosphor. The increased color purity refers to the improved red emission.

Several red phosphors have already been developed by the research fraternity, whose chromaticity parameters with EM0.3 phosphor are compared in Table 4.7, which clearly shows that EM0.3 is a better red phosphor.

Table 3.5 Comparison table of chromaticity parameters of EM0.3 red phosphor to reported other red phosphors.

Red phosphor	**CIE coordinates**	**CCT (K)**	**Color purity (%)**	**Ref.**
$CaAlSiN_3:Eu^{2+}$	0.556, 0.329	1337	65.6	[29]
$Ba_2GeO_4:Eu^{3+}$	0.590, 0.360	1320	85.1	[160]
$KMgPO_4$: Eu^{3+} & Sm^{3+}	0.610, 0.381	1324	97.4	[49]
$SrMoO_4:Sm^{3+}$	0.575, 0.419	1691	98.4	[135]
$Sr_2MgSi2O_7:Eu^{3+}$	0.550, 0.445	2004	98.5	[89]
$Cr_2MgSi_2O_7:Eu^{3+}$	0.555, 0.440	1934	98.7	[97]
$Sr_2lnTaO_6:Eu^{3+}$	0.625, 0.369	1202	98.9	[103]
$SrMoO_4:Sm^{3+}$ & Li^+	0.586, 0.410	1582	99.0	[135]
EM0.3 phosphor	0.674, 0.326	1000	99.9	**This work**

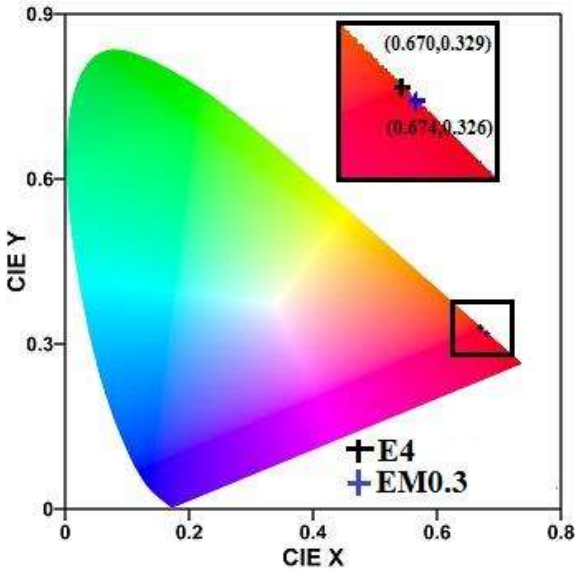

Fig. 3.12 Chromaticity diagram for E4 and EM0.3 phosphors.

3.3 Conclusions

In summary, CMO, E2, E3, E4, E5, EM0.1, EM0.3 and EM0.5 were successfully synthesized. The results of XRD and FTIR authenticate that the dopants are successfully substituted in the site of Ca^{2+}. XPS analysis validates that Ca, Mo, Eu and Mn are in +2, +6, +3 and +2 oxidation states, respectively. It is also shown that oxygen vacancies increase in the Mn-doped sample. The luminescence performance of E4 is examined by co-doing Mn^{2+}. In our study, it is observed that with proper concentration tuning of Mn^{2+} in E4, PL intensity can be increased. An increase in asymmetric parameter for EM0.3 reflects that it is a better red phosphor then every other prepared sample. Thus, our study collaborates towards building very low-cost red-emitting phosphor for white LEDs applications.